Defect Modulation via SnX₂ Additives in FASnI₃ Perovskite Solar Cells

Syed Joy, ¹ Tareq Hossain, ¹ Adam Tichy, ² Stephen Johnson, ² and Kenneth R. Graham^{1,*}

¹Department of Chemistry, University of Kentucky, Lexington, Kentucky 40506, USA.

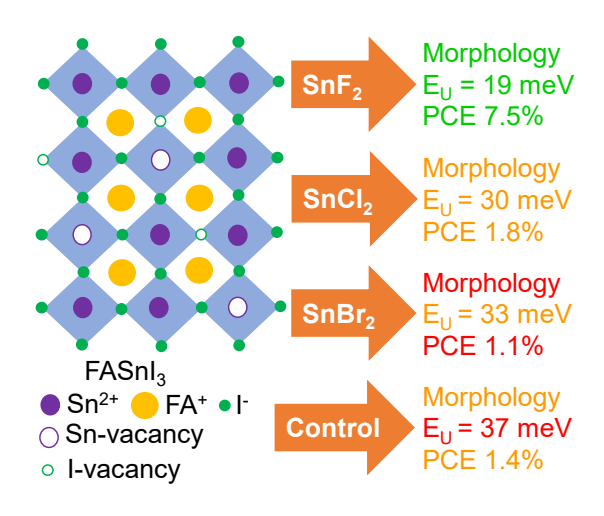
²Department of Physics, Transylvania University, Lexington, Kentucky 40508, USA.

Corresponding Author

*Kenneth R. Graham. E-mail: kenneth.graham@uky.edu

ABSTRACT Tin halide perovskites suffer from high defect densities compared to their lead counterparts. To decrease defect densities, SnF₂ is commonly used as an additive in tin halide perovskites. Herein, we investigate how SnF₂ compares to other SnX₂ additives (X=F, Cl, Br) in terms of electronic and ionic defect properties in FASnI₃. We find that FASnI₃ films with SnF₂ show the lowest Urbach energies (*E*_U) of 19 meV and decreased p-type character, as probed with ultraviolet photoemission spectroscopy. The activation energy of ion migration, as probed with thermal admittance spectroscopy, for FASnI₃ with SnF₂ is 1.33 eV, which is higher than with SnCl₂ and SnBr₂, which are 1.22 eV and 0.79 eV, respectively, resulting in less ion migration. Due to improved defect passivation, the champion power conversion efficiency of FASnI₃ with SnF₂ is 7.47% and only 1.84% and 1.12% with SnCl₂ and SnBr₂, respectively.

TOC GRAPHIC



KEYWORDS: Tin halide perovskite, additives, defects, ion migration, solar cell

Tin halide perovskites (Sn-HPs) have emerged as promising alternatives to lead halide perovskites (Pb-HPs). Sn-HPs have comparable optoelectronic properties to Pb-HPs, including a narrower band gap of ~1.3-1.4 eV that is more ideal for single-junction solar cells, low exciton binding energies, and relatively high charge-carrier mobility, while also being less toxic than Pb. 1-⁶ The record power conversion efficiency (PCE) for Sn-HPs is now 14.8%,⁷ which is still significantly lower than their Pb-containing counterparts. The main reason for the inferior efficiency of Sn-HPs is ascribed to the instability of the Sn²⁺ oxidation state in Sn-HPs, with minimal amounts of oxygen and/or dimethyl sulfoxide (DMSO) solvent often leading to oxidation to Sn⁴⁺ even in an inert glovebox atmosphere.⁸⁻¹⁰ Consequently, Sn⁴⁺ species, *i.e.* SnI₄, an oxidation product of SnI₂, causes the release of two holes to the valence band in Sn-HPs, resulting in self-ptype doping characteristics with increased background hole density of ~10²⁰ cm⁻³. ^{11, 12} In Sn-HPs it is also known that surface defects such as tin vacancies (V_{Sn}), caused by the formation of SnI₄ at the surface or grain boundaries, are thermodynamically stable and detrimental to device performance and stability. 13-15 The increased defect states at the surface, triggered by SnI₄, act as electron traps and centers for non-radiative recombination.¹⁶

Numerous approaches have thus been adopted to retard Sn²⁺ oxidation, including additives that act as anti-oxidants or passivate surfaces,¹⁷⁻¹⁹ mixed A-site cations that increase stability,²⁰ mixed dimensional 3D/2D phases that impede moisture ingression,²¹⁻²³ and alternative solvent systems that do not oxidize Sn²⁺.^{24, 25} The most ubiquitous additive used in pure Sn and mixed Sn-Pb perovskites is SnF₂. The incorporation of SnF₂ into Sn-HPs precursor solution improves the substrate coverage, film morphology, and photovoltaic performance.²⁶⁻²⁸ However, SnCl₂ and

 $SnBr_2$ can play a similar role as SnF_2 , including improving crystallization dynamics as well as decreasing V_{Sn} defect concentrations, but only a few works report using $SnCl_2$ or $SnBr_2$ as additives. 18,29,30

It was previously proposed that SnF2 acts as a reducing agent, either reducing the SnI4 and/or suppressing the SnI2 oxidation by creating a Sn-rich environment, which results in decreased Sn vacancies with less background charge carrier density. 31, 32 However, Pascual et al. 27 reported that both SnF2 and SnCl2 can decrease the SnI4 concentration by undergoing halide exchange reactions with SnI4 to form SnF4 and SnCl4, respectively, that can reduce the insertion of Sn⁴⁺ into the Sn-HPs crystal lattice, leading to decreased defect states. We also showed that chloride-containing organic salts can undergo a similar halide exchange reaction with SnI4, which decreases the SnI4 concentration in solution as well as in thin films. 33 Recently, Meggiolaro et al. 34 reported that SnF2 can decrease the SnI4 concentration by forming a mixed valence Sn3F8 phase, which is thermodynamically preferred over SnF4. In addition, halide ion migration is a well-recognized problem for HPs that increases hysteresis in current-voltage scans and results in decreased device stability. 35 In addition, phase segregation is also observed in mixed-halides HPs under light or bias stress. 36, 37 However, a recent study showed that there is significantly less halide ion migration in Sn-HPs compared to Pb-HPs due to the strong Sn-halide bond. 38

While much has been done to elucidate how SnF₂ improves the electronic properties and performance of Sn-HPs, a complete picture of how SnX₂ additives with varying halides affect the electronic and ionic defect properties in FASnI₃ perovskites is still missing. Herein, we use a combination of photothermal deflection spectroscopy (PDS) and ultraviolet photoemission spectroscopy (UPS) to provide insight into defect states in FASnI₃ films fabricated with and without SnX₂ additives. The activation energies of ion migration in FASnI₃ devices are determined

using thermal admittance spectroscopy (TAS). Our results show that SnF₂ decreases energetic disorder in FASnI₃ films and decreases ion migration more than SnCl₂ and SnBr₂, while also resulting in improved film morphologies. As a result, FASnI₃ devices with SnF₂ display the highest PCE compared to devices with SnCl₂ and SnBr₂. Moreover, impurities such as SnI₄ and I₂ are intentionally introduced into the FASnI₃ precursor solution with SnF₂ as an additive, and we directly observe that SnF₂ decreases the detrimental effects of SnI₄.

To qualitatively probe halide exchange with SnX₂ additives, we prepared mixed solutions of SnI₄ with SnF₂, SnCl₂, and SnBr₂, respectively, and first examined the solution color change. As shown in Figure 1a, the red color of the initial SnI₄ solution turns colorless, yellow, or orange after the addition of SnF₂, SnCl₂, or SnBr₂, respectively, and the absorbance of SnI₄ decreases as evidenced by the UV-vis absorbance spectra (Figure S1). While readily observable color changes and UV-vis absorbance measurements provide a qualitative indicator that the SnI4 concentration is reduced upon addition of SnX₂, ¹¹⁹Sn NMR can provide a more comprehensive picture of the different Sn species in the mixed solution. Here, SnI4 shows a peak at a chemical shift of -2023 ppm while the SnI₂ peak appears at -699 ppm (Figure 1b). As previously reported,²⁷ SnI₄ is able to undergo complete halide exchange with SnF2 when mixed at 1:2 (SnI4:SnF2) mole ratio, and we observe similar results. When SnF₂ is mixed with SnI₄, there is a disappearance of the SnI₄ signal in the ¹¹⁹Sn NMR and a corresponding increase in two new peaks at -700 and -771 ppm, confirming the formation of SnF4 and SnI2. This halide exchange occurs because F is a highly electronegative anion with hard Lewis base character, and it has a greater affinity towards the harder Sn⁴⁺ Lewis acid as opposed to the softer Sn²⁺. Therefore, F⁻ replaces I⁻ from SnI₄ and forms SnF₄ and SnI₂.²⁷ Similarly, reaction with SnCl₂ completely eliminates the SnI₄ signal through the formation of Sn⁴⁺ complexes, i.e., SnCl₄ and/or SnI_xCl_y species with signals at -606, -610, -625

and -634 ppm (reference SnCl₄ peak appears at -625 ppm), and no SnI₂ is observed. When SnBr₂ is mixed with SnI₄, four signals show up at -583, -1013, -1270, and -1347 ppm (reference SnBr₄ shows two peaks at -1013 and -1270 ppm) and again no SnI₄ peak remains. However, while SnF₂ leaves no doubt that complete halide exchange to form SnI₂ and SnF₄ occurs, both SnCl₂ and SnBr₂ show evidence of incomplete halide exchange (*i.e.*, the formation of SnI_xCl_y and SnI_xBr_y, where x and y are both greater than zero).

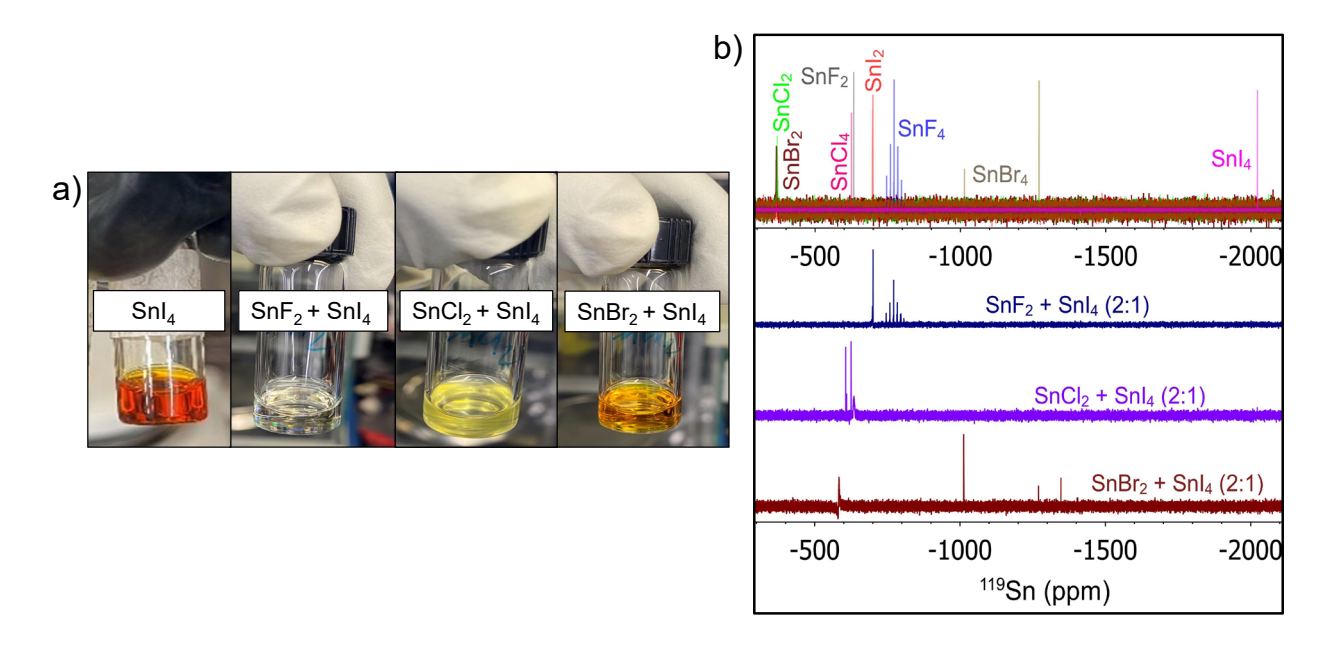


Figure 1. a) Photographic images of 0.5 M solution of reference SnI₄ and a mixture of SnF₂, SnCl₂, and SnBr₂ with SnI₄ (2:1 mole ratio), respectively, in DMSO. b) ¹¹⁹Sn NMR of the reference Sn compounds (top), and a mixture of SnF₂, SnCl₂, and SnBr₂ with SnI₄ (2:1 mole ratio), respectively, in DMSO-*d*₆.

With a clear picture of solution behavior, we next turn to understand how different SnX₂ additives affect the FASnI₃ perovskite thin film properties. To do so, FASnI₃ was fabricated with 7.5 mol% SnX₂ additives. The XRD spectra of the resulting perovskite films show no new peaks or significant peak shifts upon the addition of SnX₂ additives compared to the reference FASnI₃

film (Figure S2). SEM images (Figure S3) show that in the case of FASnI₃ + SnF₂ the grain size increases compared to the FASnI₃ film without SnX₂ additives. This increase in grain size with SnF₂ is attributed to the ability of SnF₂ to slow the prompt nucleation of Sn-HPs, which helps increase the grain size.^{28, 39} On the contrary, FASnI₃ + SnCl₂ and FASnI₃ + SnBr₂ films exhibit similar or worse morphologies than the pristine FASnI₃ film. Here, SnCl₂ leads to similar morphologies as observed for the control while SnBr₂ results in a significantly higher pin-hole density. Since SnI₄ and I₂ are degradation products of Sn-HPs, we then intentionally added 2 mol% SnI₄ and 2 mol% I₂ to FASnI₃ + SnF₂ precursor solutions. The XRD patterns with SnI₄ or I₂ introduced show no major changes relative to the control. The SEM images show that grain sizes decrease and pinhole densities increase upon addition of SnI₄, and with I₂ the grain sizes and pinhole densities are similar to the pristine FASnI₃ film.

To quantify how the SnX₂ additives impact disorder at the band-edge in the FASnI₃ thin films, we carried out PDS measurements, as shown in Figure 2a. The Urbach energy ($E_{\rm U}$) is evaluated from the exponential function of the decaying absorption onset tail at the band edge, ⁴⁰ and provides a quantitative measurement of energetic disorder at and near the band edge. The lower the $E_{\rm U}$ value, the less energetic disorder is present. The pristine FASnI₃ film shows an $E_{\rm U}$ of 37 meV, which decreases to 19 meV with SnF₂. The $E_{\rm U}$ of FASnI₃ with SnCl₂ and SnBr₂ are 30 and 33 meV, respectively, which are significantly higher than the FASnI₃ + SnF₂ film but less than the pristine FASnI₃ film. Therefore, all SnX₂ additives decrease electronic disorder at the band-edge, with SnF₂ proving more effective than SnCl₂ and SnBr₂. When an intentional impurity of 2% SnI₄ is added to the FASnI₃ + SnF₂ solution, the resulting $E_{\rm U}$ of the film increases to 26 meV. This $E_{\rm U}$ is still significantly lower than the 37 meV observed for the film without SnF₂ and no added impurities. On the contrary, the $E_{\rm U}$ is further increased to 47 meV after adding 2% I₂ to the FASnI₃

+ SnF₂ solution. It is reported that when I₂ is formed during the degradation of Sn-HPs, it facilitates the further oxidation of SnI₂.^{8,41} As a result, I₂ addition consumes SnI₂ from the precursor solution and makes the solution more Sn deficient as compared to when SnI₄ is added. This increased Sn deficiency could result in increased V_{Sn} and/or Frenkel pair type defects, leading to more energetic disorder in the material.

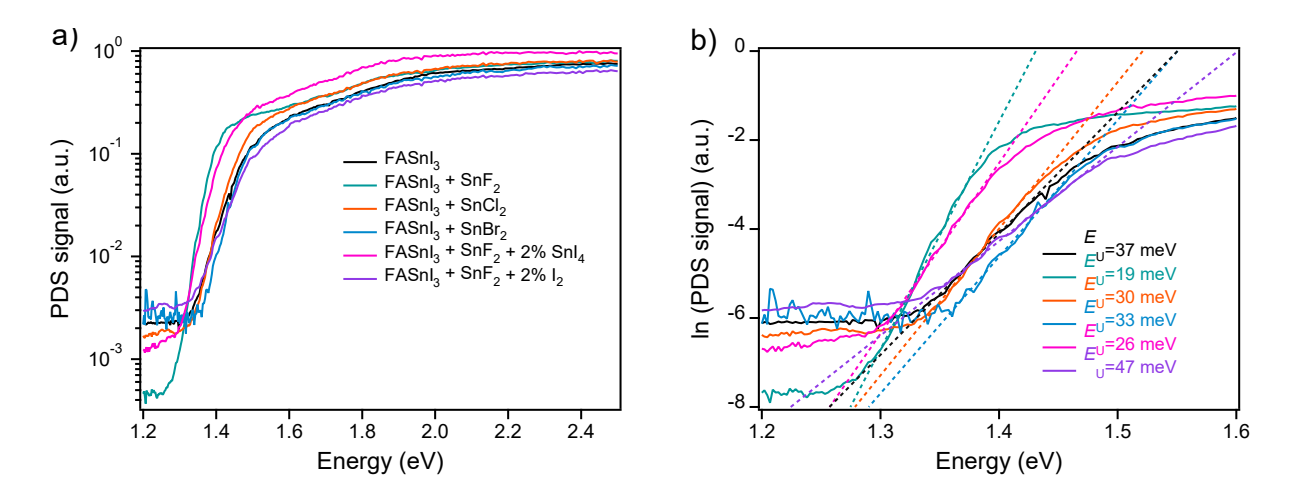


Figure 2. PDS spectra on a semi-log plot (a) and after taking the natural log of the PDS signal (b) to extract the Urbach energy (E_U) of FASnI₃, FASnI₃ + SnF₂, FASnI₃ + SnCl₂, FASnI₃ + SnBr₂, FASnI₃ + SnF₂ + 2% SnI₄, and FASnI₃ + SnF₂ + 2% I₂ films.

The PDS spectra also show that the absorption onset of the FASnI₃ + SnF₂ film red shifts by 60 meV with respect to the pristine FASnI₃ film. The red shift of this absorbance onset for the FASnI₃ + SnF₂ film is also confirmed by the UV-vis absorbance spectra (Figure S4). On the other hand, FASnI₃ films with SnCl₂ and SnBr₂ show similar absorption onsets as the pristine FASnI₃ film. The increased Sn⁴⁺-related defects likely induce more lattice distortion, which increases the optical gap. These trends are consistent with the Urbach energies and suggest that Sn⁴⁺associated defects increase the optical gap.

Photoluminescence (PL) measurements were carried out to gain insight into radiative and nonradiative recombination dynamics. All films are prepared on glass substrates for PL measurements to avoid quenching by the electrodes or transport layers. As shown in Figure S5a and b, the PL intensity of FASnI₃ + SnF₂ is 6.6 times higher than pristine FASnI₃, which is consistent with decreased non-radiative recombination at defect sites following SnF₂ addition. Also, the emission peak of FASnI₃ + SnF₂ film red shifts by \sim 15 nm and the full-width half maxima (FWHM) decreases from 82 nm to 70 nm compared to the pristine FASnI₃ film. In contrast, the PL intensities of FASnI₃ with SnCl₂ and SnBr₂ are more comparable to pristine FASnI₃, with SnCl₂ and SnBr₂ showing slightly increased and decreased emission intensity, respectively, relative to pristine FASnI₃. Furthermore, the FWHM with SnCl₂ and SnBr₂ is 79 and 73 nm, respectively, which are narrower than pristine FASnI₃ and wider than with SnF₂. The emission peaks with SnCl₂ and SnBr₂ blue shift by 9 nm compared to pristine FASnI₃. Considering that the Urbach energies with SnCl₂ and SnBr₂ are lower than the pristine FASnI₃, we suspect the blueshift in emission may be due to a small amount of Cl and Br incorporation into the FASnI₃ lattice. This Cl or Br incorporation is consistent with the (001) plane peak shift to slightly higher diffraction angle with SnCl₂ and SnBr₂ addition (see Figure S2b). Similar to the PDS results, it appears that the 2% SnI₄ impurity addition is compensated by the presence of SnF₂, as it shows higher PL intensity and slightly redshifted emission compared to the pristine FASnI₃ film. On the other hand, the emission peak with 2% I₂ is much broader with FWHM of ~95 nm and the intensity is ~2 times lower than the control FASnI₃ film.

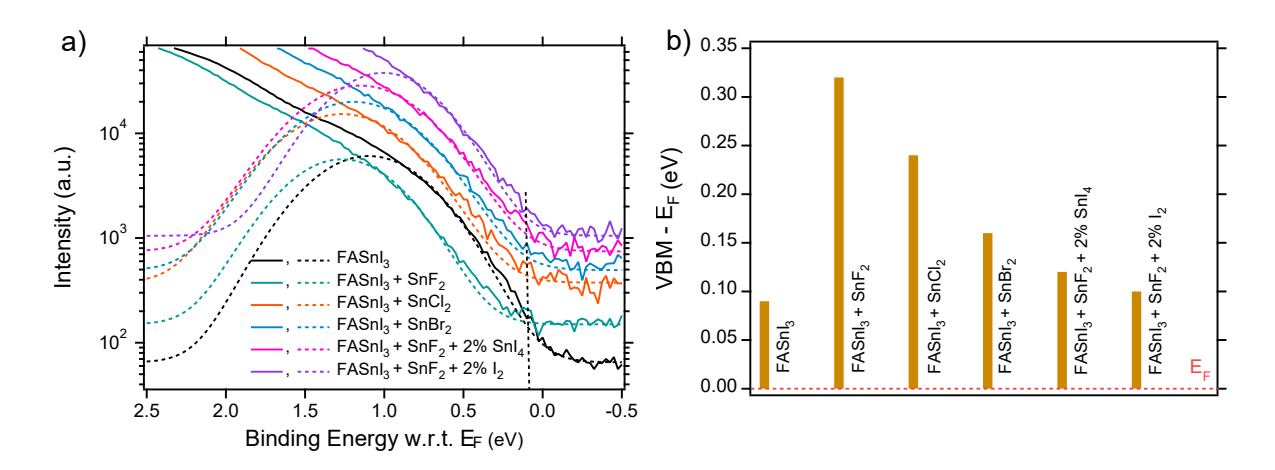


Figure 3. a) UPS spectra zoomed into the valence band maxima (VBM) region with the Gaussian fits used to extract the VBM onset energy displayed (dashed lines) and b) difference between the VBM and Fermi energy (E_F).

Ultraviolet photoemission spectroscopy (UPS) can provide insight into the p-type characteristic of the respective Sn-HP films. Here, more Sn⁴⁺ in the film will lead to more p-type character as the p-type charge carriers (holes) increase with increasing Sn⁴⁺ in FASnI₃. The extent of p-type doping is related to the energy difference between the valence band maximum (VBM) and the Fermi energy (E_F), where this energy difference decreases as the amount of p-type charge-carriers increases. The pristine FASnI₃ film without any additives shows a WF of 4.60 eV and VBM of 0.09 eV vs. E_F (Figure 3, SI Figure S6 and Table S1). The Sn⁴⁺ and Sn²⁺ content determined by X-ray photoelectron spectroscopy (XPS) is 8.2% and 91.8%, respectively, in the pristine FASnI₃ film (Figure S7 and Table S2). In the case of FASnI₃ + SnF₂, a deeper WF of 4.73 eV is determined and the VBM lies 0.32 eV away from E_F, which confirms that SnF₂ decreases the p-type character of the FASnI₃ film. The XPS spectra confirm that the Sn⁴⁺ content decreases upon SnF₂ addition, with the FASnI₃ + SnF₂ film displaying a Sn⁴⁺ concentration of 6.1% as compared to 8.2% for the control film in the near-surface region. In the case of FASnI₃ with SnCl₂ and SnBr₂, the difference between the VBM and E_F is greater than for pristine FASnI₃ and less than with SnF₂. These trends

further support that SnCl₂ and SnBr₂ both play a role in passivating Sn⁴⁺ associated defects, yet both are less effective than SnF₂. Surprisingly, the addition of 2% SnI₄ and 2% I₂ to the FASnI₃+SnF₂ solution leads to more p-type character and higher Sn⁴⁺ concentrations of 13.5% and 12.8%, respectively. Additionally, the addition of both SnCl₂ and SnBr₂ increase the Sn⁴⁺ content detected by XPS. Such increases in Sn⁴⁺ relative to pristine FASnI₃ does not agree with the PDS and PL intensity trends, which could be attributed to differences between the film surface probed by XPS and UPS and the bulk film probed by PDS and PL. For example, we expect that the majority of Sn⁴⁺ is at the film surface or at grain boundaries, as theoretical calculations indicate that Sn⁴⁺formation is unfavorable in the bulk and highly favorable at the surface.^{11, 13, 27}

To understand how electronic defects impact the FASnI₃ photovoltaic (PV) devices with and without SnX_2 additives, fabricated with we p-i-n devices ITO/PEDOT:PSS/FASnI₃/ICBA/BCP/Ag structure. The current density-voltage (J-V) plots and statistical distributions of PV performance of the corresponding devices are shown in Figure 4a-e. The best performing control FASnI₃ device without SnX₂ additives has a PCE of 1.39% (average of forward and reverse scans), with a J_{SC} , V_{OC} , and FF of 5.22 mA·cm⁻², 0.520 V, and 0.513, respectively (Table 1). In the case of the FASnI₃ + SnF₂ devices, the best performing device shows a J_{SC} of 17.5 mA·cm⁻², V_{OC} of 0.641 V, and FF of 0.665 and thus a PCE of 7.47% (average of forward and reverse scans), which corresponds with the decrease in defect states observed upon SnF₂ addition. On the contrary, the best performing cells with SnCl₂ and SnBr₂ show PCEs close to the control device, with PCEs of 1.84% and 1.20%, respectively. Such results are comparable to previous Sn-HP devices, where devices with SnCl₂ and SnBr₂ as additives reach PCEs of 2.71 and 0.35%, respectively.³⁰ The improvement in PCE with SnCl₂ relative to the control may be attributed to the lower energetic disorder and decreased p-type character, while the decreased

average performance with SnBr₂ compared to the control likely stems from the poor film morphology.

There are multiple reports on halide perovskite devices where there is a correlation between *E*_U and *V*_{OC} deficit along with their PV performance. ^{40, 42, 43} We observe a similar trend, with the *V*_{OC} of FASnI₃ + SnF₂ surpassing the V_{OC} of the pristine FASnI₃ devices and the devices with SnCl₂ and SnBr₂. Moreover, large grain sizes and fewer grain boundaries lead to less non-radiative recombination and higher shunt resistance, resulting in higher *J*_{SC}, *V*_{OC}, and FF of FASnI₃ + SnF₂ device. In the case of FASnI₃ with SnCl₂ and SnBr₂, smaller grains and higher pinhole densities relative to with SnF₂, as seen from SEM images (Figure S3), likely contribute further to the decreased PV performance. In general, the much more pronounced PCE increase with SnF₂ arises from the culmination of multiple beneficial effects, including the complete conversion of SnI₄ to SnF₄, significantly decreased energetic disorder observed with PDS, largest decrease in p-type character, greatest proportion of radiative emission, and uniform film morphologies with increased grain sizes.

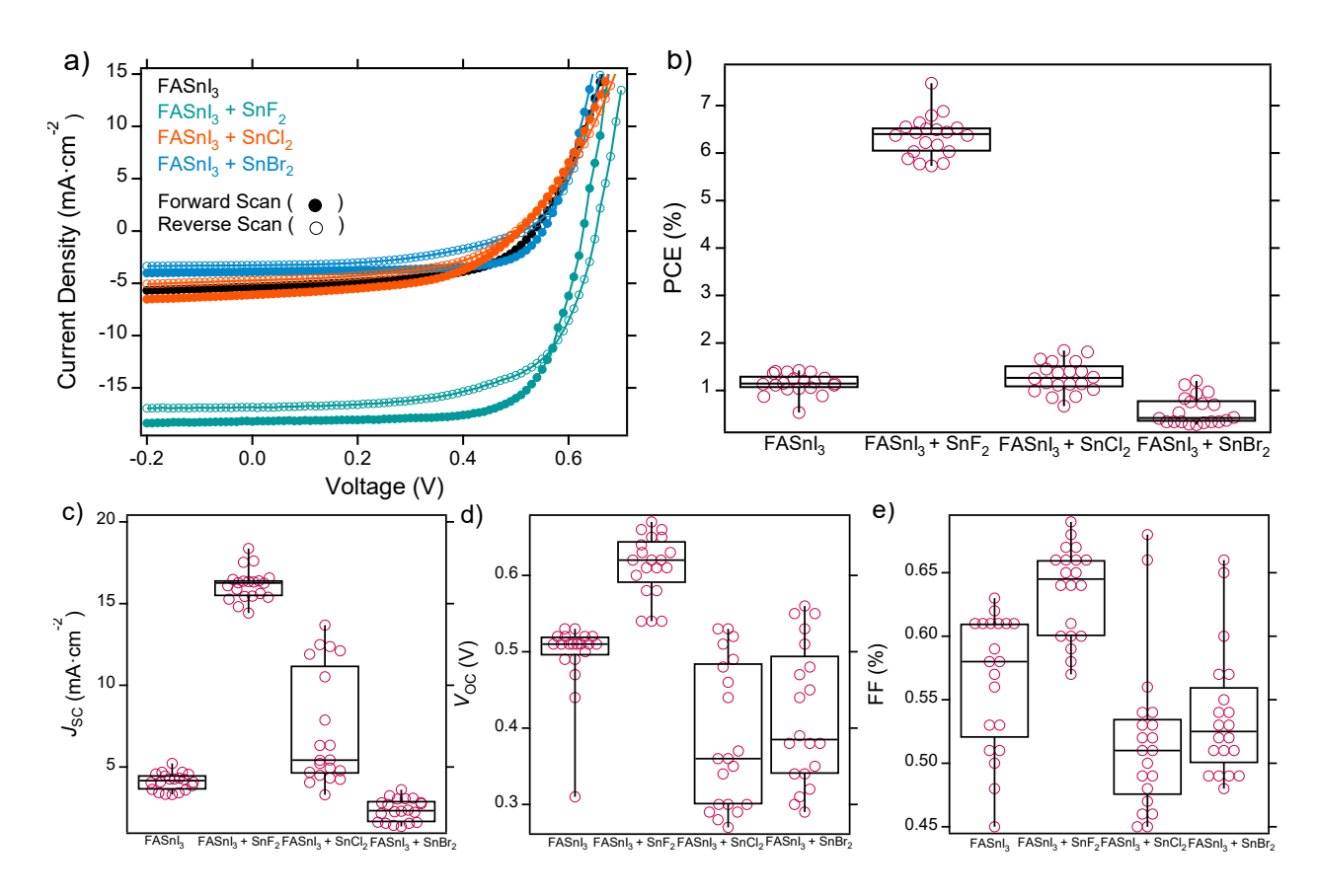


Figure 4. a) Current density-voltage (J-V) plots, and statistical distributions of b) power conversion efficiency (PCE), c) short-circuit current (J_{SC}) , d) open-circuit voltage (V_{OC}) , and e) fill factor (FF) for FASnI₃, FASnI₃ + SnF₂, FASnI₃ + SnCl₂, and FASnI₃ + SnBr₂ devices.

Table 1. Photovoltaic performance

Samples		$J_{\rm SC}$ (mA·cm ⁻²)	Voc (V)	FF	PCE (%)
FASnI ₃	Average*	4.09±0.54	0.494±0.050	0.561±0.058	1.15±0.24
$FASnI_3 + SnF_2$	Average	16.1±1.2	0.612±0.041	0.634±0.047	6.35±0.76
FASnI ₃ + SnCl ₂	Average	7.22±3.43	0.388±0.132	0.516±0.086	1.28±0.56
FASnI ₃ + SnBr ₂	Average	2.37±0.68	0.414±0.117	0.535±0.082	0.575±0.333

^{*}Average value is calculated from the forward and reverse scans of 20 devices.

To calculate the carrier concentration in FASnI₃ PV cells with and without SnX₂ additives, the capacitance-voltage (C-V) measurement was performed using the Mott-Schottky approach according to the following equation⁴⁴:

$$\frac{1}{C^2} = \frac{2(V_{bi} - V)}{e \varepsilon_0 \varepsilon_r N_i} \tag{1}$$

where C is the measured capacitance, V is the applied voltage, $V_{\rm bi}$ is the built-in voltage, e is the elementary charge, ε_0 is the vacuum permittivity, ε_r is the dielectric constant of perovskite material, and N_i is the intrinsic carrier density. By fitting equation (1) in the Mott-Schottky plot (Figure S8b), the built-in potential (V_{bi}) and intrinsic carrier density (N_i) are extracted. The V_{bi} extracted for the FASnI₃ + SnF₂, FASnI₃ + SnCl₂, and FASnI₃ + SnBr₂ devices is 0.63, 0.54, and 0.47 V, respectively. The calculated N_i of FASnI₃ + SnF₂, FASnI₃ + SnCl₂, and FASnI₃ + SnBr₂ devices is 9.05×10^{15} , 1.38×10^{16} , and 1.11×10^{16} cm⁻³, respectively, which are comparable to the literature values determined by capacitance and Hall measurements. ^{24, 26, 45-47} The lower N_i of FASnI₃ + SnF₂ relative to with SnCl₂ and SnBr₂ supports that the formation of Sn⁴⁺ is most suppressed, leading to less background carriers (holes) and lower defect densities, which agrees with the UPS and XPS measurements. Dark J-V measurements (Figure S9) also support the decreased hole density, with decreased dark current densities for FASnI₃ + SnF₂ compared to with other SnX₂ additives. The higher V_{bi} and decreased N_i of FASnI₃ + SnF₂ device is expected to lead to better charge extraction and decreased charge carrier recombination, which is consistent with the enhanced J_{SC}, V_{OC}, and FF.

Thermal admittance spectroscopy was carried out to determine the activation energy (E_a) for ion migration in the devices, as shown in Figure 5. Notably, we attribute the TAS signals to ionic migration as opposed to electronic trapping and detrapping based on recent work with Pb-HPs performed by the Deibel group.⁴⁸ The emission rate is directly related to the applied frequency (f),

and E_a is calculated from the slope of the Arrhenius plot (details are included in the SI). For the pristine FASnI₃ device (Figure 5a and b, Figure S11a), two ionic defect species with E_{a1} of 1.05 eV and E_{a2} of 0.24 eV are determined. In the case of the FASnI₃ + SnF₂ device (Figure 5 c and d, Figure S11b), E_a is increased to 1.33 eV, indicating that ionic migration will be decreased during device operation. We find a similar E_a of 1.29 eV for FASnI₃ + SnCl₂ (Figure S12). In contrast, the lowest E_a of 0.79 eV is found for FASnI₃ + SnBr₂ (Figure S13).

Insight into the nature of the defects can be inferred from previous computational results. $^{14, 49}$ Here, V_{Sn} is the dominant defect (*i.e.*, it has the lowest formation energy) under Sn-poor conditions and V_I has the lowest formation energy under Sn-rich conditions. 49 It is reported that the energy barrier for migration of V_{Sn} and V_I is 2.40 eV and <0.60 eV, respectively. $^{50, 51}$ Our TAS measurements, with an E_{a1} of 1.05 eV and E_{a2} of 0.24 eV, are approximately half of these calculated values and are tentatively attributed to V_{Sn} and V_I , respectively. X-ray photoemission spectroscopy indicates that the FASnI3 film with no additive is Sn deficient, with a N:Sn:I ratio of 2.2:1:3.4 (Table S4); however, when SnF2 is added the stoichiometry becomes nearly ideal at 2.0:1:2.9. The V_{Sn} concentration should therefore decrease upon addition of SnF2. The E_a for V_{Sn} in the FASnI3 + SnF2 sample increases to 1.33 eV. A similar stoichiometry is observed with SnCl2, and a similarly high E_a is also observed. On the other hand, the E_a with SnBr2 is reduced to even less than pristine FASnI3, even though the stoichiometry is closer to ideal (2.1:1:3.1) than pristine FASnI3.

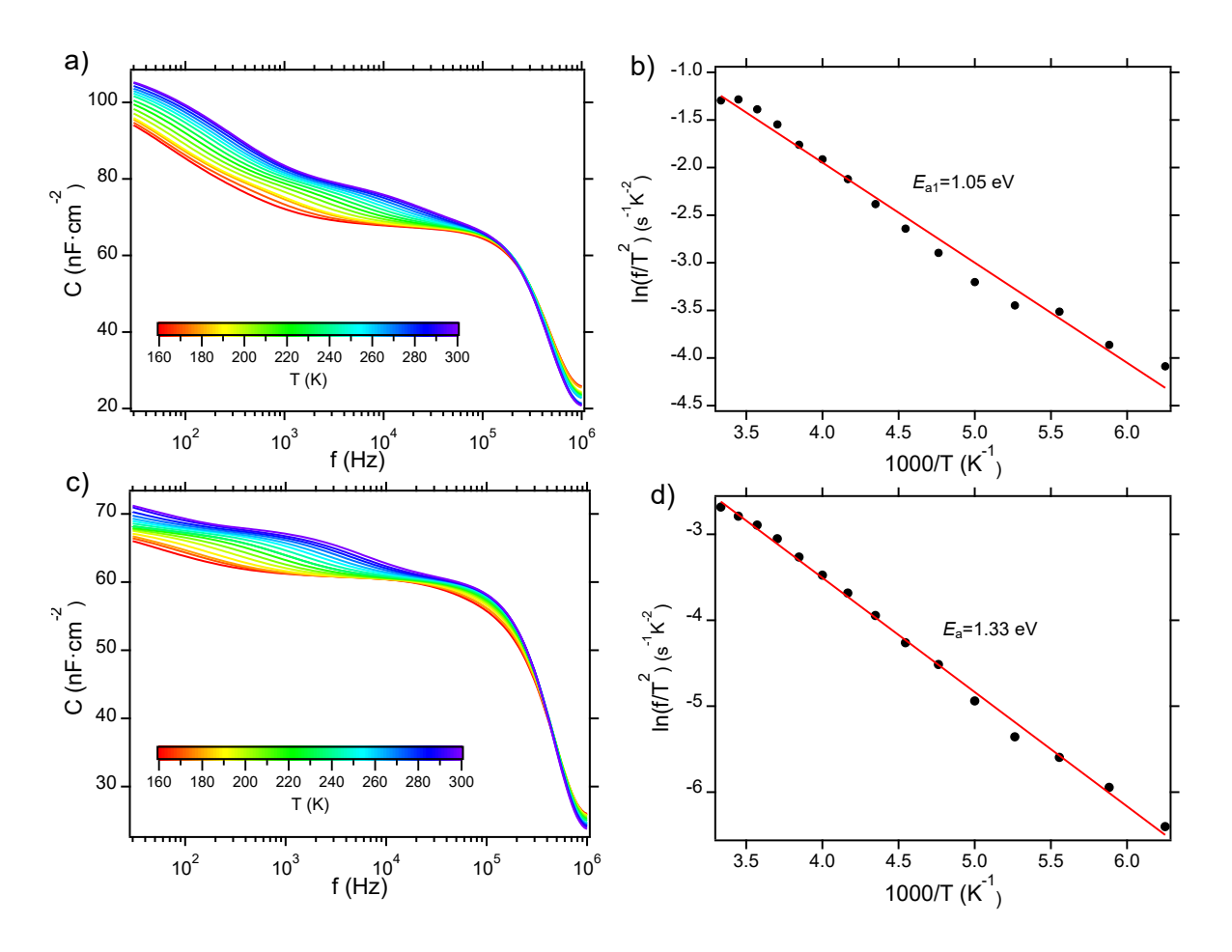


Figure 5. Capacitance-frequency (C-f) plots from TAS measurements a) FASnI₃ and c) FASnI₃ + SnF₂ devices carried out under dark conditions between 160 and 300 K at 0 V DC bias with an AC bias amplitude of 10 mV. Activation energy (*E*_a) of the ionic defects of b) FASnI₃ and d) FASnI₃ + SnF₂ devices extracted from Arrhenius plots of the characteristic peak frequency, obtained from the differential capacitance (-f.dC/df) at various temperatures.

In summary, the work presented here identifies the role of SnX₂ additives on electronic and ionic defects in FASnI₃ perovskite solar cells. The beneficial role of the SnF₂ additive in FASnI₃ can be attributed to improved morphology, less energetic disorder, and decreased Sn⁴⁺ associated defects in the film, whereas these benefits are significantly decreased with SnCl₂ and SnBr₂ additives. Here, the formation of SnF₄ through the halide exchange reaction with SnI₄ prevents the insertion

of Sn^{4+} into the crystal lattice, which retards the self p-type doping and decreases the background hole density and dark current. Moreover, the activation energy of ion migration increases upon SnF_2 addition, which could be attributed to the strong Sn-F bond and its effect on passivating grain boundaries as well as the decreased concentration of Sn^{4+} . Consequently, the photovoltaic performance of $FASnI_3 + SnF_2$ is significantly improved relative to the control and the other SnX_2 additives.

ASSOCIATED CONTENT

Supporting Information. Experimental methods, UV-vis absorbance spectra, PL spectra, SEM

images, UPS and XPS spectra, C-V plots, dark J-V plots, device data, and TAS data.

AUTHOR INFORMATION

Corresponding Author

Kenneth R. Graham - Department of Chemistry, University of Kentucky, Lexington, Kentucky

40506, USA; E-mail: Kenneth.graham@uky.edu

Notes

The authors declare no competing financial interests.

ACKNOWLEDGMENT

S. Joy, A. T., S. Johnson, and K.R.G. acknowledge support from the National Science Foundation

under cooperative agreement No. 1849213. T.H. and K.R.G. also acknowledge support from the

National Science Foundation under DMR-2102257. The authors thank Olajumoke Oladele and

Prof. Anne-Frances Miller for performing NMR measurements and Kiera Draffen for assistance

with PDS measurements.

18

References

- (1) Liu, H.; Zhang, Z.; Zuo, W.; Roy, R.; Li, M.; Byranvand, M. M.; Saliba, M. Pure Tin Halide Perovskite Solar Cells: Focusing on Preparation and Strategies. *Adv. Energy Mater.* **2022**, *13* (3).
- (2) Tong, J.; Jiang, Q.; Ferguson, A. J.; Palmstrom, A. F.; Wang, X.; Hao, J.; Dunfield, S. P.; Louks, A. E.; Harvey, S. P.; Li, C.; et al. Carrier Control in Sn–Pb Perovskites via 2D Cation Engineering for All-Perovskite Tandem Solar Cells with Improved Efficiency and Stability. *Nat. Energy* **2022**, *7* (7), 642-651.
- (3) Hu, M.; Zhang, Y.; Gong, J.; Zhou, H.; Huang, X.; Liu, M.; Zhou, Y.; Yang, S. Surface Sn(IV) Hydrolysis Improves Inorganic Sn–Pb Perovskite Solar Cells. *ACS Energy Lett.* **2023**, *8* (2), 1035-1041.
- (4) Lanzetta, L.; Webb, T.; Marin-Beloqui, J. M.; Macdonald, T. J.; Haque, S. A. Halide Chemistry in Tin Perovskite Optoelectronics: Bottlenecks and Opportunities. *Angew. Chem. Int. Ed. Engl.* **2023**, *62* (8), e202213966.
- (5) Song, D.; Li, H.; Xu, Y.; Yu, Q. Amplifying Hole Extraction Characteristics of PEDOT:PSS via Post-treatment with Aromatic Diammonium Acetates for Tin Perovskite Solar Cells. *ACS Energy Lett.* **2023**, *8* (8), 3280-3287.
- (6) Zhao, J.; Zhang, Z.; Li, G.; Aldamasy, M. H.; Li, M.; Abate, A. Dimensional Tuning in Lead-Free Tin Halide Perovskite for Solar Cells. *Adv. Energy Mater.* **2023**, *13* (13).
- (7) Yu, B. B.; Chen, Z.; Zhu, Y.; Wang, Y.; Han, B.; Chen, G.; Zhang, X.; Du, Z.; He, Z. Heterogeneous 2D/3D Tin-Halides Perovskite Solar Cells with Certified Conversion Efficiency Breaking 14%. *Adv. Mater.* **2021**, *33* (36), e2102055.

- (8) Pascual, J.; Nasti, G.; Aldamasy, M. H.; Smith, J. A.; Flatken, M.; Phung, N.; Di Girolamo, D.; Turren-Cruz, S.-H.; Li, M.; Dallmann, A.; et al. Origin of Sn(II) Oxidation in Tin Halide Perovskites. *Mater. Adv.* **2020**, *1* (5), 1066-1070.
- (9) Saidaminov, M. I.; Spanopoulos, I.; Abed, J.; Ke, W.; Wicks, J.; Kanatzidis, M. G.; Sargent, E. H. Conventional Solvent Oxidizes Sn(II) in Perovskite Inks. *ACS Energy Lett.* **2020**, *5* (4), 1153-1155.
- (10) Hossain, T.; Joy, S.; Draffen, K.; Bright, R.; Johnson, S.; Graham, K. R. Oxidation in Tin Halide Perovskites: Influence of Acidic and Basic Additives. *ACS Appl. Energy Mater.* **2023**, *6* (24), 12334-12342.
- (11) Ricciarelli, D.; Meggiolaro, D.; Ambrosio, F.; Angelis, F. D. Instability of Tin Iodide Perovskites: Bulk p-Doping versus Surface Tin Oxidation. *ACS Energy Lett.* **2020**, *5* (9), 2787-2795.
- (12) Milot, R. L.; Klug, M. T.; Davies, C. L.; Wang, Z.; Kraus, H.; Snaith, H. J.; Johnston, M. B.; Herz, L. M. The Effects of Doping Density and Temperature on the Optoelectronic Properties of Formamidinium Tin Triiodide Thin Films. *Adv. Mater.* **2018**, *30* (44), e1804506.
- (13) Meggiolaro, D.; Ricciarelli, D.; Alasmari, A. A.; Alasmary, F. A. S.; De Angelis, F. Tin versus Lead Redox Chemistry Modulates Charge Trapping and Self-Doping in Tin/Lead Iodide Perovskites. *J. Phys. Chem. Lett.* **2020**, *11* (9), 3546-3556.
- (14) Shi, T.; Zhang, H.-S.; Meng, W.; Teng, Q.; Liu, M.; Yang, X.; Yan, Y.; Yip, H.-L.; Zhao, Y.-J. Effects of Organic Cations on the Defect Physics of Tin Halide Perovskites. *J. Mater. Chem. A* **2017**, *5* (29), 15124-15129.

- (15) Naito, T.; Takagi, M.; Tachikawa, M.; Yamashita, K.; Shimazaki, T. Theoretical Study of the Molecular Passivation Effect of Lewis Base/Acid on Lead-Free Tin Perovskite Surface Defects. *J. Phys. Chem. Lett.* **2023**, *14* (29), 6695-6701.
- (16) Treglia, A.; Ambrosio, F.; Martani, S.; Folpini, G.; Barker, A. J.; Albaqami, M. D.; De Angelis, F.; Poli, I.; Petrozza, A. Effect of Electronic Doping and Traps on Carrier Dynamics in Tin Halide Perovskites. *Mater. Horizon* **2022**, *9* (6), 1763-1773.
- (17) Liu, H.; Wang, L.; Li, R.; Shi, B.; Wang, P.; Zhao, Y.; Zhang, X. Modulated Crystallization and Reduced Voc Deficit of Mixed Lead–Tin Perovskite Solar Cells with Antioxidant Caffeic Acid. *ACS Energy Lett.* **2021**, *6* (8), 2907-2916.
- (18) Wang, T.; Tai, Q.; Guo, X.; Cao, J.; Liu, C.-K.; Wang, N.; Shen, D.; Zhu, Y.; Lee, C.-S.; Yan, F. Highly Air-Stable Tin-Based Perovskite Solar Cells through Grain-Surface Protection by Gallic Acid. *ACS Energy Lett.* **2020**, *5* (6), 1741-1749.
- (19) Tai, Q.; Guo, X.; Tang, G.; You, P.; Ng, T. W.; Shen, D.; Cao, J.; Liu, C. K.; Wang, N.; Zhu, Y.; et al. Antioxidant Grain Passivation for Air-Stable Tin-Based Perovskite Solar Cells. *Angew. Chem. Int. Ed. Engl.* **2019**, *58* (3), 806-810.
- (20) Zhou, J.; Hao, M.; Zhang, Y.; Ma, X.; Dong, J.; Lu, F.; Wang, J.; Wang, N.; Zhou, Y. Chemo-Thermal Surface Dedoping for High-Performance Tin Perovskite Solar Cells. *Matter* **2022**, *5* (2), 683-693.
- (21) Jiang, X.; Li, H.; Zhou, Q.; Wei, Q.; Wei, M.; Jiang, L.; Wang, Z.; Peng, Z.; Wang, F.; Zang, Z.; et al. One-Step Synthesis of SnI₂.(DMSO)_x Adducts for High-Performance Tin Perovskite Solar Cells. *J. Am. Chem. Soc.* **2021**, *143* (29), 10970-10976.

- (22) Jokar, E.; Cheng, P.-Y.; Lin, C.-Y.; Narra, S.; Shahbazi, S.; Diau, E. W.-G. Enhanced Performance and Stability of 3D/2D Tin Perovskite Solar Cells Fabricated with a Sequential Solution Deposition. *ACS Energy Lett.* **2021**, *6* (2), 485-492.
- (23) Wang, F.; Jiang, X.; Chen, H.; Shang, Y.; Liu, H.; Wei, J.; Zhou, W.; He, H.; Liu, W.; Ning, Z. 2D-Quasi-2D-3D Hierarchy Structure for Tin Perovskite Solar Cells with Enhanced Efficiency and Stability. *Joule* **2018**, *2*, 2732-2743.
- (24) Nasti, G.; Aldamasy, M. H.; Flatken, M. A.; Musto, P.; Matczak, P.; Dallmann, A.; Hoell, A.; Musiienko, A.; Hempel, H.; Aktas, E.; et al. Pyridine Controlled Tin Perovskite Crystallization. *ACS Energy. Lett.* **2022**, *7* (10), 3197-3203.
- (25) Aktas, E.; Poli, I.; Ponti, C.; Li, G.; Olivati, A.; Girolamo, D. D.; Alharthi, F. A.; Li, M.; Polamares, E.; Petrozza, A.; et al. One-Step Solution Deposition of Tin-Perovskite onto a Self-Assembled Monolayer with a DMSO-Free Solvent System. *ACS Energy Lett.* **2023**, *8*, 5170-5174. (26) Kumar, M. H.; Dharani, S.; Leong, W. L.; Boix, P. P.; Prabhakar, R. R.; Baikie, T.; Shi, C.; Ding, H.; Ramesh, R.; Asta, M.; et al. Lead-free Halide Perovskite Solar Cells with High Photocurrents Realized through Vacancy Modulation. *Adv. Mater.* **2014**, *26* (41), 7122-7127.
- (27) Pascual, J. F., M.; Félix, R.; Li, G.; Turren-Cruz, S.-H.; Aldamasy, M. H.; Hartmann, C.; Li, M.; Girolamo, D. D.; Nasti, G.; Hüsam, E.; Wilks, R. G.; Dallmann, A.; Bär, M.; Hoell, A.; Abate, A. Fluoride Chemistry in Tin Halide Perovskites. *Angew. Chem. Int. Ed.* **2021**, *60*, 21583 21591. (28) Liao, W.; Zhao, D.; Yu, Y.; Grice, C. R.; Wang, C.; Cimaroli, A. J.; Schulz, P.; Meng, W.; Zhu, K.; Xiong, R. G.; et al. Lead-Free Inverted Planar Formamidinium Tin Triiodide Perovskite

Solar Cells Achieving Power Conversion Efficiencies up to 6.22%. *Adv. Mater.* **2016**, *28* (42), 9333-9340.

- (29) Liu, X.; Wang, Y.; Wu, T.; He, X.; Meng, X.; Barbaud, J.; Chen, H.; Segawa, H.; Yang, X.; Han, L. Efficient and Stable Tin Perovskite Solar Cells Enabled by Amorphous-Polycrystalline Structure. *Nat. Comm.* **2020**, *11* (1), 2678.
- (30) Marshall, K. P.; Walker, M.; Walton, R. I.; Hatton, R. A. Enhanced Stability and Efficiency in Hole-Transport-Layer-Free CsSnI₃ Perovskite Photovoltaics. *Nat. Energy* **2016**, *1* (12), 16178.
- (31) Chen, Q.; Luo, J.; He, R.; Lai, H.; Ren, S.; Jiang, Y.; Wan, Z.; Wang, W.; Hao, X.; Wang, Y.; et al. Unveiling Roles of Tin Fluoride Additives in High-Efficiency Low-Bandgap Mixed Tin-Lead Perovskite Solar Cells. *Adv. Energy Mater.* **2021**, *11* (29), 2101045.
- (32) Gupta, S.; Cahen, D.; Hodes, G. How SnF₂ Impacts the Material Properties of Lead-Free Tin Perovskites. *J. Phys. Chem. C* **2018**, *122* (25), 13926-13936.
- (33) Joy, S.; Atapattu, H. R.; Sorensen, S.; Pruett, H.; Olivelli, A. B.; Huckaba, A. J.; Miller, A.-F.; Graham, K. R. How Additives for Tin Halide Perovskites Influence the Sn⁴⁺ Concentration. *J. Mater. Chem. A* **2022**, *10* (25), 13278-13285.
- (34) Meggiolaro, D.; Gregori, L.; De Angelis, F. Formation of a Mixed Valence Sn₃F₈ Phase May Explain the SnF₂ Stabilizing Role in Tin-Halide Perovskites. *ACS Energy Lett.* **2023**, *8* (5), 2373-2375.
- (35) Sakhatskyi, K.; John, R. A.; Guerrero, A.; Tsarev, S.; Sabisch, S.; Das, T.; Matt, G. J.; Yakunin, S.; Cherniukh, I.; Kotyrba, M.; et al. Assessing the Drawbacks and Benefits of Ion Migration in Lead Halide Perovskites. *ACS Energy Lett.* **2022**, *7*, 3401-3414.
- (36) Brennan, M. C.; Draguta, S.; Kamat, P. V.; Kuno, M. Light-Induced Anion Phase Segregation in Mixed Halide Perovskites. *ACS Energy Lett.* **2018**, *3*, 204-213.

- (37) Xiao, Z.; Zhao, L.; Tran, N. L.; Lin, Y. L.; Silver, S. H.; Kerner, R. A.; Yao, N.; Kahn, A.; Scholes, G. D.; Rand, B. P. Mixed-Halide Perovskites with Stabilized Bandgaps. *Nano Lett.* **2017**, 17, 6863-6869.
- (38) Ighodalo, K. O.; Chen, W.; Liang, Z.; Shi, Y.; Chu, S.; Zhang, Y.; Khan, R.; Zhou, H.; Pan, X.; Ye, J.; et al. Negligible Ion Migration in Tin-Based and Tin-Doped Perovskites. *Angew. Chem. Int. Ed.* **2023**, *62* (5), e202213932.
- (39) Xiao, M.; Gu, S.; Zhu, P.; Tang, M.; Zhu, W.; Lin, R.; Chen, C.; Xu, W.; Yu, T.; Zhu, J. Tin-Based Perovskite with Improved Coverage and Crystallinity through Tin-Fluoride-Assisted Heterogeneous Nucleation. *Adv. Optical Mater.* **2017**, *6* (1), 1700615.
- (40) Subedi, B. L., C.; Chen, C.; Liu, D.; Junda, M. M.; Song, Z.; Yan, Y.; Podraza, N. J. Urbach Energy and Open-Circuit Voltage Deficit for Mixed Anion–Cation Perovskite Solar Cells. *ACS Appl. Mater. Interfaces* **2022**, *14*, 7796-7804.
- (41) Lanzetta, L.; Webb, T.; Zibouche, N.; Liang, X.; Ding, D.; Min, G.; Westbrook, R. J. E.; Gaggio, B.; Macdonald, T. J.; Islam, M. S.; et al. Degradation Mechanism of Hybrid Tin-based Perovskite Solar Cells and the Critical Role of Tin (IV) Iodide. *Nat. Comm.* **2021**, *12* (1), 2853.
- (42) Ledinsky, M.; Schonfeldova, T.; Holovsky, J.; Aydin, E.; Hajkova, Z.; Landova, L.; Neykova, N.; Fejfar, A.; Wolf, S. D. Temperature Dependence of the Urbach Energy in Lead Iodide Perovskites. *J. Phys. Chem. Lett.* **2019**, *10* (6), 1368-1373.
- (43) Mahesh, S.; Ball, J. M.; Oliver, R. D. J.; McMeekin, D. P.; Nayak, P. K.; Johnston, M. B.; Snaith, H. J. Revealing the Origin of Voltage Loss in Mixed-Halide Perovskite Solar Cells. *Energy Environ. Sci.* **2020**, *13* (1), 258-267.
- (44) Reichert, S.; An, Q.; Woo, Y. W.; Walsh, A.; Vaynzof, Y.; Deibel, C. Probing the Ionic Defect Landscape in Halide Perovskite Solar Cells. *Nat. Comm.* **2020**, *11* (1), 6098.

- (45) Lee, S. J.; Shin, S. S.; Im, J.; Ahn, T. K.; Noh, J. H.; Jeon, N. J.; Seok, S. I.; Seo, J. Reducing Carrier Density in Formamidinium Tin Perovskites and Its Beneficial Effects on Stability and Efficiency of Peorvskite Solar Cells. *ACS Energy Lett.* **2018**, *3*, 46-53.
- (46) Ke, W.; Stoumpos, C. C.; Spanopoulos, I.; Chen, M.; Wasielewski, M. R.; Kanatzidis, M. G. Diammonium Cations in the FASnI₃ Perovskite Structure Lead to Lower Dark Currents and More Efficient Solar Cells. *ACS Energy Lett.* **2018**, *3* (7), 1470-1476.
- (47) Khadka, D. B.; Shirai, Y.; Yanagida, M.; Tadano, T.; Miyano, K. Alleviating Defect and Oxidation in Tin Perovskite Solar Cells Using a Bidentate Ligand. *Chem. Mater.* **2023**, *35* (11), 4250-4258.
- (48) Futscher, M. H.; Deibel, C. Defect Spectroscopy in Halide Perovskites Is Dominated by Ionic Rather than Electronic Defects. *ACS Energy Lett.* **2021**, *7* (1), 140-144.
- (49) Zhang, Z.; Huang, Y.; Wang, C.; Jiang, Y.; Jin, J.; Xu, J.; Li, Z.; Su, Z.; Zhou, Q.; Zhu, J.; et al. Green-Antisolvent-Regulated Distribution of P-type Self-Doping Enables Tin Perovskite Solar Cells with An Efficiency of Over 14%. *Energy Environ. Sci.* **2023**, *16* (8), 3430-3440.
- (50) Zhou, S.; Zhu, S.; Guan, J.; Wang, R.; Zheng, W.; Gao, P.; Lu, X. Confronting the Air Instability of Cesium Tin Halide Perovskites by Metal Ion Incorporation. *J. Phys. Chem. Lett.* **2021**, *12* (45), 10996-11004.
- (51) Eames, C.; Frost, J. M.; Barnes, P. R.; O'Regan, B. C.; Walsh, A.; Islam, M. S. Ionic Transport in Hybrid Lead Iodide Perovskite Solar Cells. *Nat. Comm.* **2015**, *6*, 7497.